



OPEN

High density deposits of binary colloids

Hyoeyun Kim^{1,2,3,4}, Marta Gonçalves^{1,4}, Sung Hoon Kang³✉ & Byung Mook Weon^{1,2}✉

Colloids are essential materials for modern inkjet printing and coating technology. For printing and coating, it is desirable to have a high density of colloids with uniformity. Binary colloids, which consist of different size colloidal particles, have the potential to achieve high coating density and uniformity from size effects. We report a strategy to attain high-density deposits of binary colloids with uniform, crack-free, and symmetric deposits through droplet evaporation on micropillar arrays. We modify surfaces of micropillar arrays with plasma treatment to control their surface energy and investigate how binary colloidal fluids turn into well-controlled deposits during evaporation with X-ray microscopic and tomographic characterizations. We attribute temporary surface energy modification of micropillar arrays to the well-controlled high-density final deposits. This simple, low-cost, and scalable strategy would provide a viable way to get high-quality, high-density deposits of colloids for various applications.

Colloidal suspensions that consist of insoluble colloidal particles in a solvent are the main component of inkjet printing, a remarkably economical technique used for device manufacturing in several industries (i.e. optoelectronics, energy storage, tissue engineering, biodetection/sensing)^{1–6}. Besides the economic advantage of inkjet printing, additional benefits come from the easy control of inkjet materials, delivering exact quantities of nanoinks through single ink droplets on pre-fabricated substrate patterns, and rendering specific structures and properties⁷. From a physical viewpoint, colloidal suspensions, including insoluble colloidal particles with diameters of approximately 1 nm to several μm are considered a model of nanoinks^{8,9}. The drying process of colloidal nanoinks is critical in achieving uniform deposition of colloidal particles but challenging in industrial applications because of coffee-ring effect, characterized by solute segregation at the contact line of evaporating colloidal droplets¹⁰, and crack formation, which is induced by air invasion into the deposits^{11,12}. Both results cause nonuniform and defective deposition of colloids and eventually degrade the electrical and optical properties of deposits. Additionally, the evaporation of monodispersed colloidal nanoinks inevitably causes the generation of empty spaces among spherical colloidal particles¹³. The maximum packing density from monodispersed spherical particles is 74% when particles are arranged with face-centered or hexagonal closed packing, a crystalline state. The maximum packing density of a monodisperse particles with random packing is 64%¹⁴. In binary colloidal particles with two different diameters, small particles are expected to fill in empty space among large particles, increasing the packing fraction and generating a more physically stable deposition^{15,16}. The increment of packing fraction by using bimodal particles, which leads to highly-dense deposits in the inkjet printing technique, has been shown to enhance electrical and sensing properties of printed devices effectively^{17–19}. Finding appropriate deposition condition of binary colloids is crucial to improve coating density and uniformity of colloidal nanoinks deposits.

Achieving uniform deposition of monodispersed colloids through evaporation is essential in recent studies^{20,21}, including a micropillar-guided deposition⁹. Due to surface roughness, hydrophobicity of substrates^{22–26} would induce the self-pinning of colloidal fluids on micropillar substrates. A constant contact angle mode (CCA) during droplet evaporation would cause preferential accumulation of colloidal particles at the droplet center and eventually bump formation, as demonstrated in Fig. 1A. The existence of the bump at the droplet center results in the structural nonuniformity and instability responsible for the destruction and dysfunction of deposits. To prevent the bump formation from monodispersed colloids, we suggest a surface-modified micropillar-guided deposition for binary colloids to achieve uniform crack-free high-density deposition. As the surface energy controls droplet dynamics, controlling surface energy can provide opportunities to control deposition. The surface

¹Soft Matter Physics Laboratory, School of Advanced Materials Science and Engineering, SKKU Advanced Institute of Nanotechnology (SAINT), Sungkyunkwan University, Suwon 16419, South Korea. ²Research Center for Advanced Materials Technology, Sungkyunkwan University, Suwon 16419, South Korea. ³Department of Mechanical Engineering and Hopkins Extreme Materials Institute, Johns Hopkins University, Baltimore, MD 21218, USA. ⁴These authors contributed equally: Hyoeyun Kim and Marta Gonçalves. ✉email: shkang@jhu.edu; bmweon@skku.edu

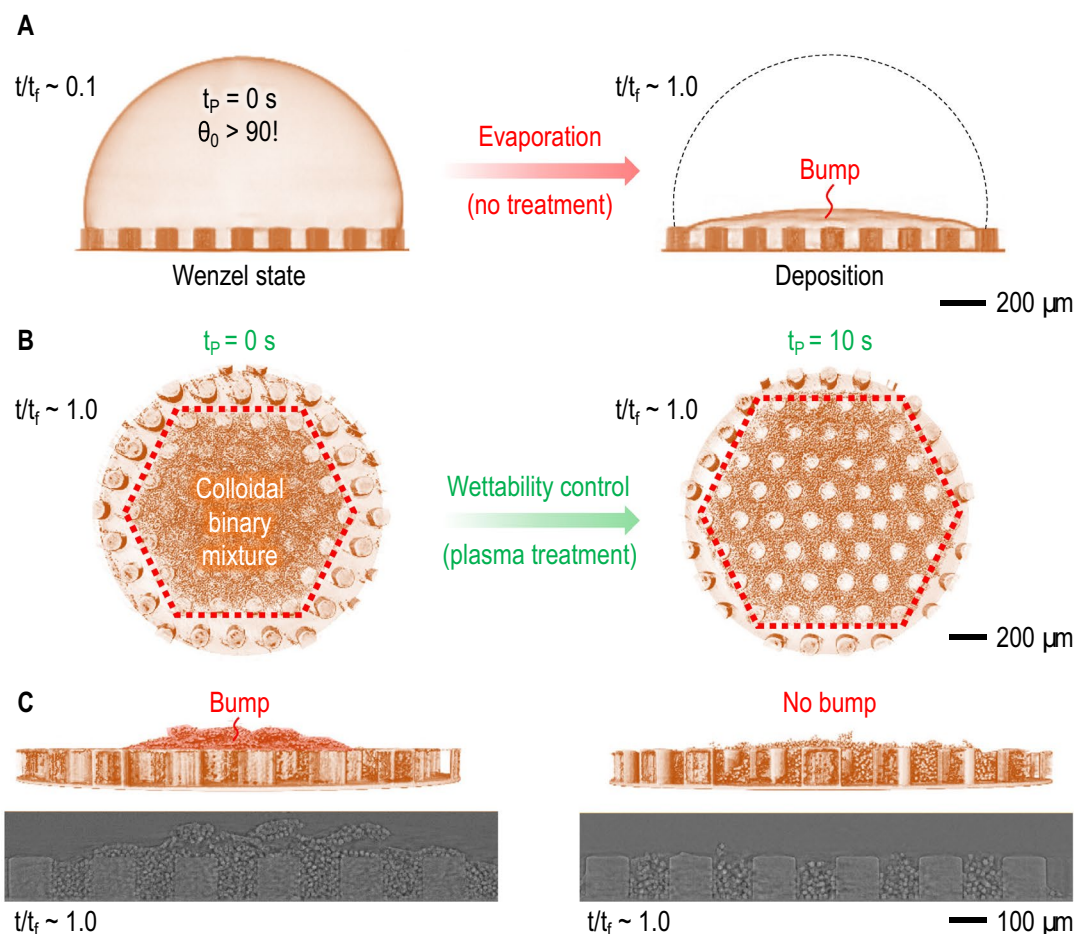


Figure 1. X-ray microtomography of evaporation-mediated deposition of binary colloids. (A) Starting colloidal droplets on PDMS micropillar patterns (left: at initial time $t/t_f \sim 0.1$ (t_f = evaporation complete time) with no treatment (initial contact angle $\theta_0 > 90^\circ$, showing Wenzel wetting state) results in bump formation after evaporation (right: at final time $t/t_f \sim 1.0$). (B) By adopting plasma treatment for wettability control of micropillar patterns (plasma treatment time: $t_p = 10$ s), symmetrically hexagonal-shaped uniform deposits are achieved after evaporation ($t/t_f \sim 1.0$). (C) Bump formation after evaporation ($t/t_f \sim 1.0$) is successfully prevented by adopting wettability control of micropillar patterns, as proven by the side-view (upper) and the cross-sectional (lower) images. All images generated with Amira software (version 2019.3).

energy of the specimen is increased with plasma treatment, which increases the OH-terminal bonds^{27,28} and can induce the depinning of colloidal droplets on micropillar substrates, as demonstrated in Fig. 1B. The increasing surface energy spreads the droplet to pass through the pillar barriers, by which colloids can flow outward to the contact line. Eventually, the bump formation is successfully prevented by enhancing the surface wettability of micropillar substrates, as demonstrated in Fig. 1C.

This study demonstrates how to achieve symmetrically uniform crack-free hexagonal dense deposits of binary colloids using a surface-modified micropillar-guided deposition. Using high-resolution X-ray microtomography, we measure real-time dynamics of evaporation and deposition processes for binary colloidal droplets on plasma-modified micropillar substrates. Our findings contribute to identify the optimal conditions that are feasible in inkjet printing technology.

Materials and methods

We examined two kinds of PDMS (polydimethylsiloxane) substrates for comparison: PDMS with flat surfaces and PDMS with micropillar patterns. The PDMS substrates were fabricated with SYLGARD™ 184 Silicone Elastomer Kit (Dow, USA) at a 10:1 ratio of polymer base to cross-linking curing agent. The PDMS substrates with micropillar patterns were fabricated using a silicon wafer master mold etched with the negative structure for cylindrical pillars arranged in a hexagonal pattern. The final geometry of the micropillar array was fixed in three dimensions: pillar diameter (D_p) = 100 μm ; pillar height (H_p) = 100 μm ; pillar pitch (P_p) = 100 μm (see Fig. S1 of Supplemental Material). The pillar dimensions were chosen for optimal wetting modes, Wenzel modes, while ensuring polygonal depositions^{9,29}. For the wettability control, the surface energy was increased by applying

oxygen plasma treatment²⁷. The plasma surface activation process was carried out with a Basic Plasma Cleaner (PDC-32G-2, Harrick, USA) at a radio frequency (RF) power setting of low (7.2W). The plasma treatment time (t_p) was increased from 5 to 25 s to determine the optimum surface energy.

An aqueous binary colloidal suspension was prepared by mixing 5.0 ± 0.1 vol% polystyrene particles of $2 \mu\text{m}$ (small particles) and $10 \mu\text{m}$ (large particles) (Polysciences, USA), showing a size ratio (ω_s) to be 5 (large/small). Colloidal suspensions of polystyrene particles are widely used as model systems for inkjet printing studies^{9,30,31}. Their surface chemistry is well controlled to be completely immersed and uniformly dispersed in solvents by the supplier. The basic knowledge taken from model particles would be useful in inkjet printing, despite differences in surface chemistry and ink formulation details. Overcoming a limit of monodispersed colloids, binary colloids with significantly different diameters would contribute to dense packing (Figs. S2, S3 of Supplemental Material). Tiny droplets with the initial volumes of $1.5 \pm 0.2 \mu\text{L}$ were carefully delivered with a micropipette on the PDMS substrates with different surface energies. The side-view optical images for contact angle measurements were acquired using a drop shape analyzer (DSA25, Krüss, Germany). A digital upright microscope (VHX-700FE, Keyence, Japan) was used to visualize the droplet's temporal evolution and the final deposited pattern. Scanning electron microscopy (SEM) (S-3000H, Hitachi, Japan) was used to image the final binary colloidal deposits on the pillar substrate.

For in-situ observation of the evaporation process and visualization of the final deposited pattern of binary colloidal drops on micropillar patterned PDMS, high-resolution and high-speed X-ray imaging technique was employed in this study, allowing the acquisition of three-dimensional (3D) images through microtomography. The experiments were carried out at the 6C Bio Medical Imaging (BMI) beamline established in the Pohang Light Source (PLS-II), where the beam is composed of monochromatic synchrotron X-rays with 20 keV energy. A $\times 10$ magnification was used, translating into an effective pixel size of $0.65 \mu\text{m}$ and a field of view of $1.70 \times 1.40 \text{ mm}^2$. For image acquisition, the sample is penetrated by the beam, followed by X-ray conversion into visible light by the scintillator (LuAG:Ce $50 \mu\text{m}$) and then received by the Scientific Complementary Metal–Oxide–Semiconductor (sCMOS) camera (pco.edge) (see Fig. S4 of Supplementary Material). For 3D image acquisition, 2D projections were acquired from 0 to 180 degrees while the sample was rotating, comprising a total of 900 projections. The Octopus Reconstruction software (Octopus, Belgium) was utilized to originate 2D tomographic slices from the X-ray projection images. The Octopus software also enabled image processing by applying noise and ring filtering. The 2D slices were processed with the visualization Amira Software (Thermo Fisher Scientific, USA) to achieve the three-dimensional volume images presented in this work. The Amira software was used for noise reduction and smoothing by applying a Median Filter to the 2D tomographic slices, the Volume Rendering function for the generation of the 3D images, and the dimensions of the pillars and colloidal deposits for analysis with built-in measurement tools³².

Results and discussion

We successfully achieve highly uniform and dense deposits of binary colloids on surface-modified micropillar substrates, as described below.

Droplet pinning dynamics on a plasma-modified substrate. The initial depinning dynamics, as illustrated in Fig. 2A, is explained by surface energy modification through plasma treatment contribution, which is essential to control the initial pinning and depinning dynamics of binary colloidal fluids. Initial low surface energy or large contact angle of micropillar substrate with no treatment would be favorable for initial pinning of colloidal fluids between pillars, as demonstrated in Fig. 2B (left). Plasma treatment increases surface energy (or decrease contact angle), which is essential to induce initial depinning that makes contact lines pass through pillars, as shown in Fig. 2B (right). The temporal evolutions of pinning with no treatment and depinning with plasma treatment are shown in Fig. 2C. Surface energy modification by plasma treatment is critical for pinning or depinning dynamics at initial times.

The late re-pinning dynamics, as illustrated in Fig. 2A, is attributed to that hydrophilicity or less hydrophobicity by plasma treatment is temporary and recoverable to original hydrophobicity. Contact angle modification with plasma treatment time (t_p), as summarized in Fig. 3A, demonstrates that initial contact angles decrease by plasma treatment times for both flat and micropillar PDMS substrates. The gradual decrease of contact angles by plasma treatment times turns hydrophobicity ($\theta > 90^\circ$) into hydrophilicity ($\theta < 90^\circ$), as demonstrated in Fig. 3B. The transition from hydrophobicity to hydrophilicity appears at $t_p \sim 5$ s for flat PDMS and at $t_p \sim 15$ s for micropillar PDMS. Most importantly, hydrophilicity or less hydrophobicity with plasma treatment is not permanent. Hydrophilicity is therefore recovered to hydrophobicity, as observed in Fig. 3C. The recovery of oxygen plasma treatment is well known as aging effect^{33–37}. Original hydrophilicity is favorable for initial depinning, contributing to flattening the upper bump. Late recovery from hydrophilicity to hydrophobicity is favorable for re-pinning, minimizing the final deposit surface area.

The recovery dynamics of oxygen plasma treatment by aging effects is due to air exposure under ambient conditions ($22 \pm 3^\circ\text{C}$ room temperature and $35 \pm 5\%$ relative humidity). The longer plasma treatment time leads to a longer recovery time. In particular, micropillar PDMS substrates for $t_p = 5$ s and $t_p = 10$ s is fully recovered to $\theta_0 \sim 120^\circ$, 20 min after plasma treatment. During the evaporation process, the droplet coverage prevents the local hydrophilicity transition on the liquid–solid interface by avoiding the substrate contact with air³⁴. However, the air exposure allows the surrounding substrate to be prone to induce the aging effect, facilitating the recovery dynamics. The recovery dynamics of micropillar substrates are responsible for the late re-pinning dynamics and thus the final minimum deposit surface area.

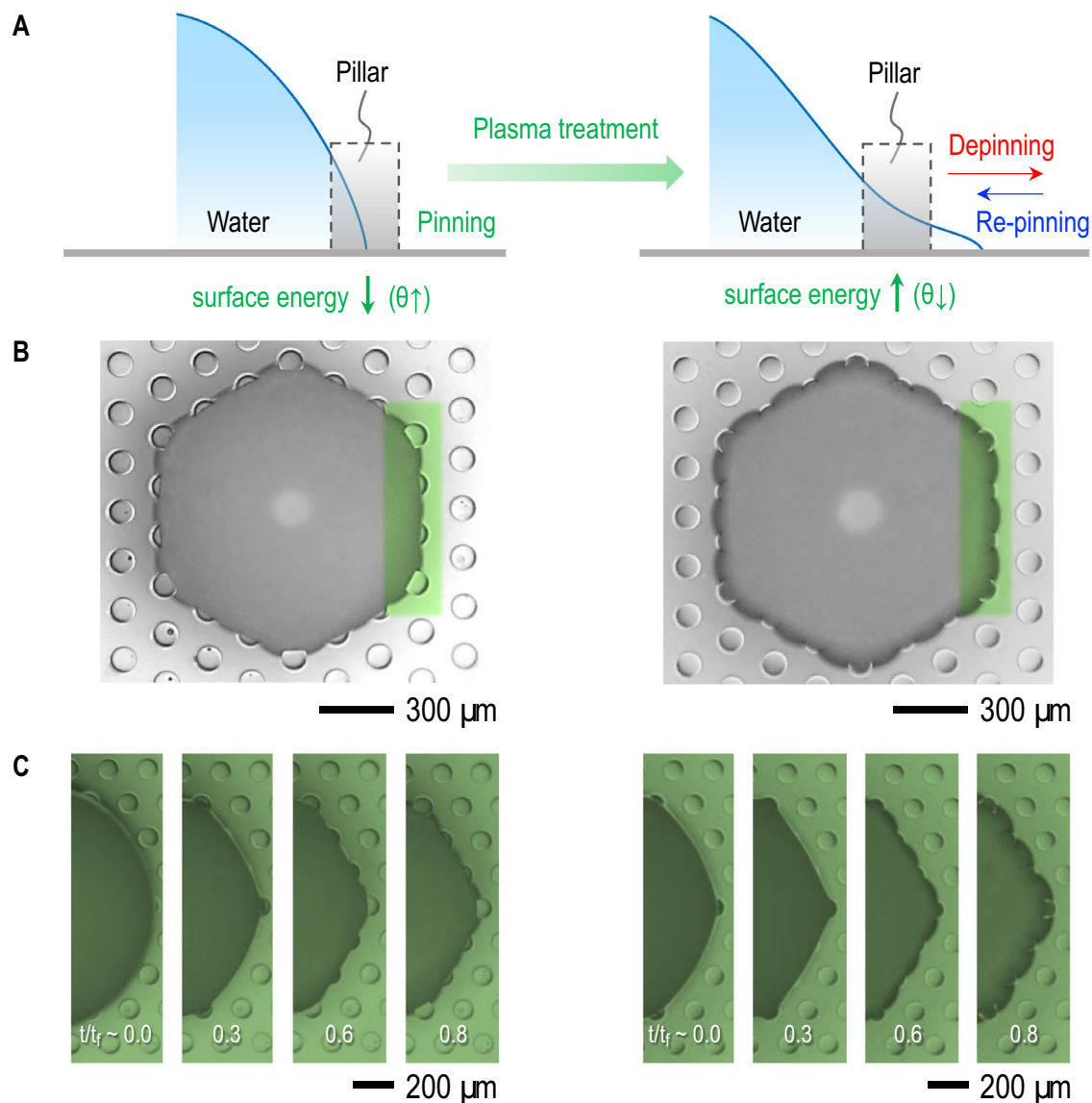


Figure 2. Pinning, depinning, and re-pinning dynamics of samples with and without surface modification through plasma treatment. **(A)** Initial low surface energy (or large contact angle) substrates is favorable for pinning of colloidal fluids between pillars (left) and plasma treatment to increase surface energy or decrease contact angle of substrates is essential for depinning to pass through between pillars (right). The final deposit shape is determined by re-pinning of the contact line. **(B)** Optical microscopic images for no treatment (left) and plasma treatment for 10 s (right) (both images were taken at $t/t_f \sim 0.7$) demonstrate contributions of pinning (left) and depinning (right) between pillars (Acquired with VHX-700FE, Keyence). **(C)** Temporal evolution of pinning by no treatment (left) and of depinning and re-pinning by plasma treatment for 10 s (right).

Achieving highly-dense uniform deposits from binary colloids. The high-density packing of binary colloids requires the uniformity of the deposition. An appropriate mixture of binary colloids is expected to realize a high-density coating if small particles sufficiently fill the space between large particles¹⁶. The size ratio (ω_s) and the mixing volume ratio (ω_m) between small and large particles are essential to obtain the highest packing density. For a colloidal mixture that displays binary particle dynamics, it is necessary to have a size ratio larger than 1.4¹⁵. We find low-density deposition by monodispersed-like behaviors at small size ratios and size separation (Figs. S3, S5 of Supplemental Material). Size separation for evaporating droplets, including binary colloids, can be induced due to hydrodynamics by diffusion force during evaporation¹⁰. We choose the size ratio to be $\omega_s = 5.0$ (= 5/1 = large/small) and the mixing volume ratio to be $\omega_m = 0.5$ (= large/total) to achieve dense, uniform and crack-free deposits.

For the specified conditions and without plasma treatment ($t_p = 0$ s), the bump formation will be present, depicting a higher height (H) of the deposit due to the highly constricted surface area of the hexagonal prism

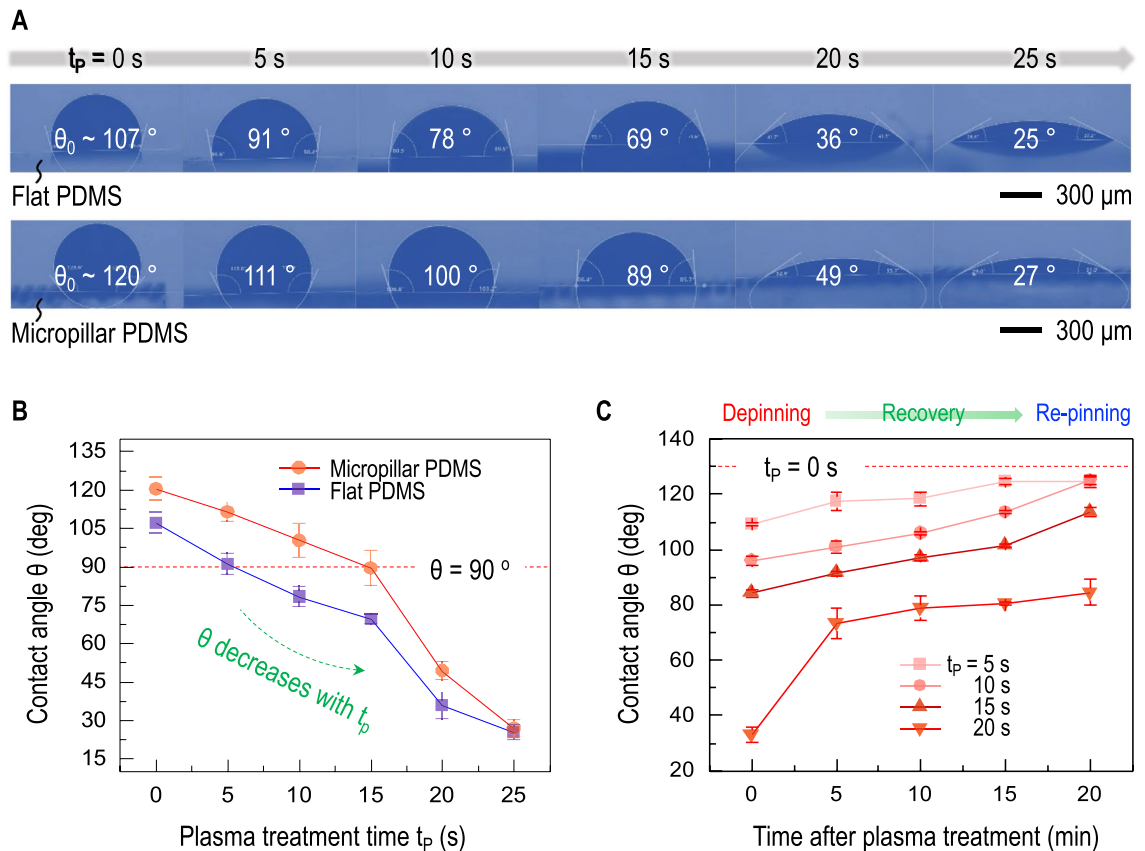


Figure 3. Wettability control with plasma treatment. **(A)** Initial contact angles decrease with increasing plasma treatment time (t_p) for both flat and micropillar PDMS (Acquired with Drop Shape Analyzer and Advance Software, Krüss Science). **(B)** Initial hydrophobicity ($\theta > 90^\circ$) turns into hydrophilicity ($\theta < 90^\circ$) at $t_p \sim 5$ s for flat PDMS and at $t_p \sim 15$ s for PDMS micropillars. **(C)** Hydrophilicity transition by plasma treatment is temporary, and recovery to hydrophobicity is shown in contact angle changes with time after plasma treatment. Early hydrophobicity is favorable for depinning, contributing to flattening the upper bump, and late recovery is favorable for re-pinning, contributing to the final deposit shape by surface area minimization.

base (S) (Fig. 4A, left). The bump formation, a failure of the uniform deposition, (Fig. 4B, left) induces the low particle density deposition of the bump layer, where large particles surrounded by small particles may behave like single-sized large particles, hindering a high-density deposition. We visualize the discontinuously arranged particles in Fig. 4B (left), which would result in poor electrical property, a weakness for inkjet-printed device fabrication³⁸. Overcoming the bump emergence is possible with plasma treatment, leading to a final pattern with uniform height, distributed through a wider surface area, effectively removing the bump and exposing the pillar top surfaces evenly, in opposition to the absence of plasma treatment (Fig. 4A, right). Here, the size of small particles is sufficiently little to fill voids between the large particles (Fig. 4B, right). Eventually, the deposit pattern can stabilize without a bump and prevent crack formation (Fig. S6 of Supplemental Material).

Hexagonal deposit patterns with geometrical uniformity can be expected by the hexagonal prism model⁹, where the hexagonal deposit volume is obtained as $V = SH$ and assuming the volume conservation principle for the total particles volumes $\phi V = \phi_0 V_0$ (the final particle packing fraction ϕ , the initial particle volume fraction ϕ_0 , and the initial droplet volume V_0). The two main parameters, S and H , are quantified in our experiments in (Fig. 4). H is taken on average from the side-view X-ray imaging, for instance, $H \sim 155 \mu\text{m}$ with bump and the average $H \sim 100 \mu\text{m}$ without bump (Fig. 1C). S is taken by subtracting the total surface areas of the pillar tops inside the hexagonal prism from the surface area of the hexagonal prism base, for instance, $S = 0.934 \text{ mm}^2$ ($= 1.075 - 0.141$) with bump and $S = 1.159 \text{ mm}^2$ ($= 1.536 - 0.377$) without bump. For both cases, $V_0 = 1.5 \text{ mm}^3$ and $\phi_0 = 0.05$. The final packing fraction of the binary colloidal deposit for the two cases can be then expected by

$$\phi = \frac{\phi_0 V_0}{SH}, \quad (1)$$

where the bump deposit pattern reveals a lower final packing fraction of $\phi = 0.52$ ($= \frac{0.05 \times 1.5}{0.934 \times 0.154}$) in comparison to the uniform deposit pattern, which accounts for a packing fraction of $\phi = 0.65$ ($= \frac{0.05 \times 1.5}{1.159 \times 0.100}$). The estimated

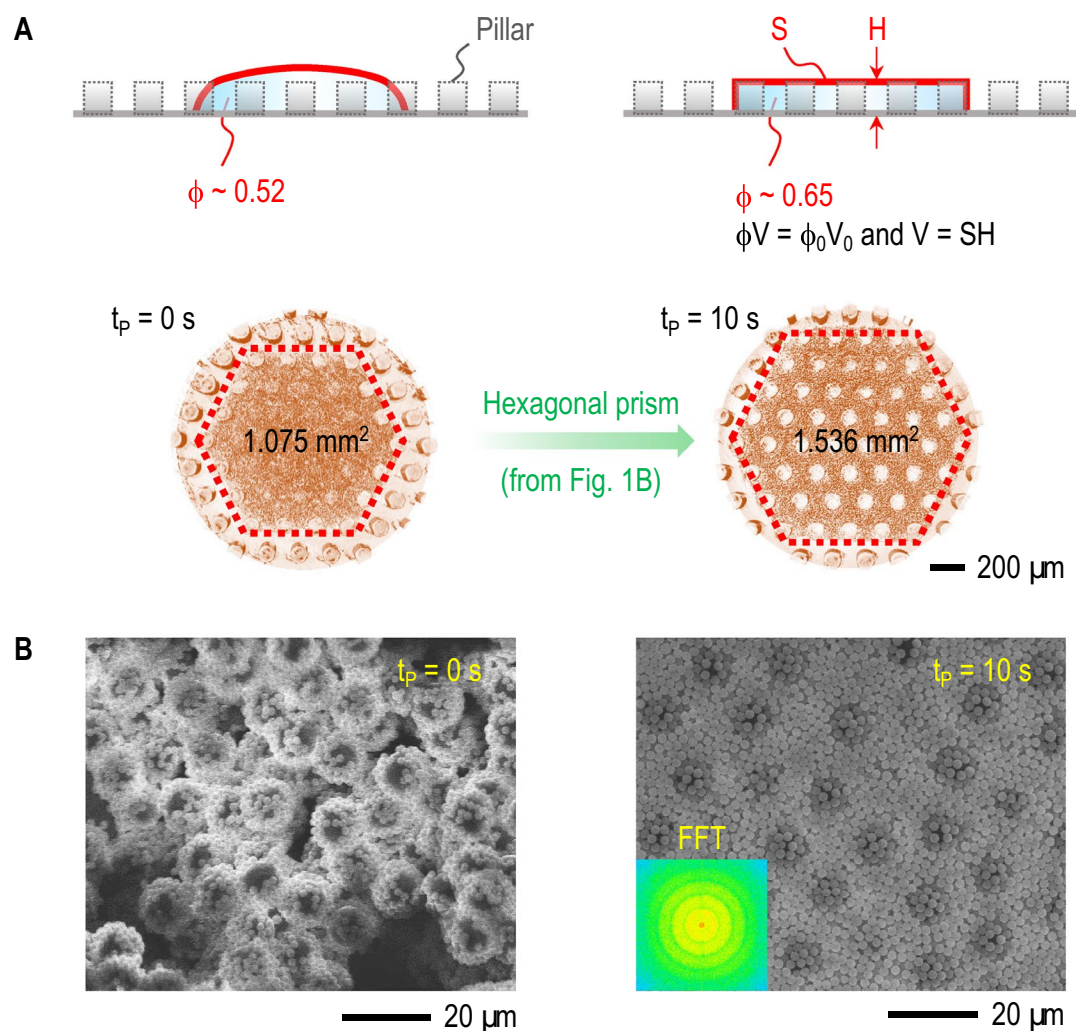


Figure 4. High-density deposition of binary colloids. (A) Schematic illustration with bump (left) and without bump (right): volume conservation ($\phi V = \phi_0 V_0$) and hexagonal prism model ($V = SH$) suggest high-density deposition of binary colloids with the final packing density $\phi \sim 0.65$ by the plasma treatment ($t_p = 10$ s) (Generated with Amira software (version 2019.3)). (B) Scanning electron microscopy (SEM) images on the deposit top layers: (left) large particles surrounded by small particles behave like single-sized large particles, and (right) small particles fill voids between large particles, creating dense packing (Acquired with S-3000H, Hitachi). The FFT (fast Fourier transform) of the right SEM image, taken by ImageJ, indicates that binary colloids build randomly packed noncrystal structures (inset). Optimal high-density packing is achieved when small and large particles are uniformly mixed by the mixing volume ratio of $\omega_m = 0.5$ (= large/total).

ϕ values reinforce the main strength of binary colloids, since ϕ is effectively increased for both cases, compared with the previous value for monodispersed deposits of $\phi = 0.48^9$.

The symmetric deposition is achieved by initial symmetric pinning, as illustrated in Fig. 5. Initial contact angles determined by plasma treatment times t_p can be larger than 90° , causing initial symmetric pinning by the capillarity predominance. This initial symmetry results in the final bilateral symmetric deposits. We often observe bump formation for $t_p = 0$ or 5 s and asymmetric deposits for $t_p = 15$ s. Consequently, initial hydrophobicity and temporal hydrophilicity transition for $t_p = 10$ s are critical to finally achieving symmetrically uniform crack-free hexagonal deposits. The complete evaporation dynamics affected by the substrate wettability attained for each t_p is represented in Fig. S7 of Supplemental Material. The attainable symmetric patterns enhance local uniformity of particles distribution, ensuring a steady packing fraction in any direction. Furthermore, this well-controlled evolution of the polygonal contact line is crucial for optimized textured surfaces in printing applications³⁹.

Optimized conditions for high-quality deposit patterns. The optimum mixtures in binary colloids are crucial to achieve highly-dense uniform patterns. The colloidal suspension, being a binary mixture of particles, has two main criteria: particle size ratio (ω_s = large particle radius divided by small particle radius) and binary mixing volume ratio (ω_m = large particle total volume divided by total particle volume). Regarding

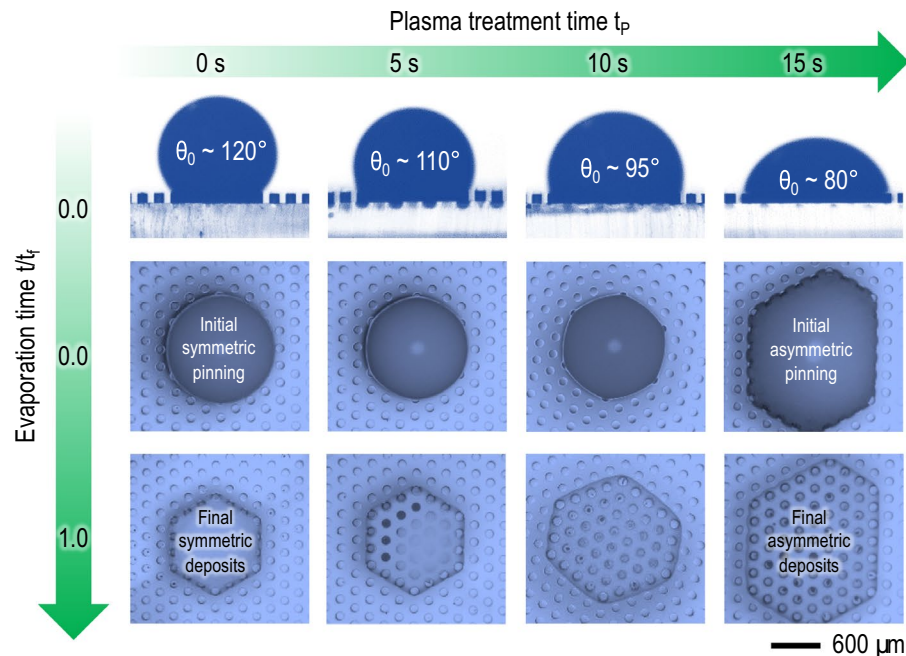


Figure 5. Symmetric deposition by initial symmetric pinning. Initial contact angles larger than 90° (upper row) are essential for initial symmetric pinning (middle row) and, therefore, final symmetric deposits (lower row) (Acquired with VHX-700FE, Keyence and Drop Shape Analyzer and Advance Software, Krüss Science).

the optimum ω_s values, to avoid the monodisperse-like behavior of larger particles, the size ratio should be $\omega_s > 1.4$ in our experiments. Simultaneously, for larger size ratios ($\omega_s > 6.46$)¹⁵, gravity can induce percolation of small particles, leading size separation (Fig. S3 of Supplemental Material). Previous experimental and theoretical studies suggest that a size ratio of $\omega_s \approx 5$ contributes to a system with more uniform distribution and low mobility allowing increased jamming, corroborating our option^{14,16}. Concerning the mixing volume ratio ω_m , a volume fraction of large particles to the total volume of dried binary particles, if smaller particles are included in a greater ratio, patterns are more prone to crack due to air invasion at the final evaporation stage (Fig. S5 of Supplemental Material)^{8,40}. Furthermore, a mixture with $\omega_m \approx 0.7$ would form a packed structure, consistent with previous works^{15,16}. However, the micropillar array hydrophobicity allied to the presence of larger particles would lead to an enhanced movement of smaller particles outwards to the drying interface, constraining the larger particles to stack at the center^{10,16,41}. The size separation at $\omega_m = 0.75$ can be a setback leading to the bump formation (Fig. S5 of Supplemental Material). Therefore, the approach of $\omega_m = 0.5$ is justified by the final goal of uniformity of the deposit.

Finally, we discuss packing fraction differences before and after plasma treatment. Our results indicate that the higher packing fraction is present for the uniform deposit pattern, consistent with the observation in Fig. 4B (right), where the pillars play the role of imprisonment leading to a cohesive pattern. In contrast, the lower packing fraction present in the bump pattern is mainly due to the size separation, displaying a non-desirable monodisperse-like behavior of larger particles (Fig. 4B, left), since smaller particles preferentially move outwards^{10,16}. Theoretically, a reachable final packing density is known as $\phi = 0.71$ for randomly packed binary colloids¹⁵, while the high-density deposits are achieved as $\phi = 0.65$ in this work. This discrepancy is due to hydrodynamics effects in evaporating droplets, where the flows disturb uniform particle distribution, which can induce colloids to be randomly packed rather than crystallized. We achieved a low packing density of 0.48 from randomly packed monodispersed colloids⁹. Therefore, binary colloids are more favorable for a high packing density than monodispersed colloids. Our finding on the deposition dynamics will be relevant to the evaporation dynamics of binary colloids, for instance, regarding evaporation dynamics on superhydrophobic surfaces⁴². Further studies are required to understand evaporation dynamics and to overcome hydrodynamic effects during evaporation to increase deposit densities.

Conclusion

Our study represents a feasible method to achieve high-quality, high-density hexagonal deposits of binary colloids on hexagonal-patterned micropillar substrates. Temporarily turning the substrates hydrophilic with oxygen plasma treatment helps to induce the initial depinning dynamics. The late recovery to hydrophobicity is helpful to induce the re-pinning dynamics of binary colloidal fluids on the substrates. These controlled dynamics would be

crucial to achieve symmetric high-density deposits of binary colloids. Additionally, the proposed method forms horizontally uniform heights by removing height differences between the center and the edge of final deposition patterns when using binary colloids and micropillar patterns. The achievable increased packing fraction imply numerous advantages for industrial performances^{43–45}. This strategy would help to optimize inkjet printing by proceeding with inexpensive, easy-fabricated, well-controlled high-density deposits of binary colloids for many possible applications, being nearly universal.

Data availability

The data that supports the findings of this study are available within the article and its Supplementary Material.

Received: 26 August 2022; Accepted: 9 December 2022

Published online: 24 December 2022

References

- Derby, B. Inkjet printing of functional and structural materials: fluid property requirements, feature stability, and resolution. *Annu. Rev. Mater. Res.* **40**, 395–414 (2010).
- Fang, Y. *et al.* Inkjet-printed vertical organic field-effect transistor arrays and their image sensors. *ACS Appl. Mater. Interfaces* **10**, 30587–30595 (2018).
- Pi, X., Zhang, L. & Yang, D. Enhancing the efficiency of multicrystalline silicon solar cells by the inkjet printing of silicon-quantum-dot ink. *J. Phys. Chem. C* **116**, 21240–21243 (2012).
- Deiner, L. J., Bezerra, C. A. G., Howell, T. G. & Powell, A. S. Digital printing of solid-state lithium-ion batteries. *Adv. Eng. Mater.* **21**, 1900737 (2019).
- Park, J. A. *et al.* Freeform micropatterning of living cells into cell culture medium using direct inkjet printing. *Sci. Rep.* **7**, 1–11 (2017).
- Singh, M., Haverinen, H. M., Dhagat, P. & Jabbour, G. E. Inkjet printing-process and its applications. *Adv. Mater.* **22**, 673–685 (2010).
- Park, J. & Moon, J. Control of colloidal particle deposit patterns within picoliter droplets ejected by ink-jet printing. *Langmuir* **22**, 3506–3513 (2006).
- Kim, J. Y., Cho, K., Ryu, S., Kim, S. Y. & Weon, B. M. Crack formation and prevention in colloidal drops. *Sci. Rep.* **5**, 1–9 (2015).
- Park, H. K., Kim, Y., Min, H., Pang, C. & Weon, B. M. Hexagonal deposits of colloidal particles. *Phys. Rev. E* **100**, 022602 (2019).
- Liu, W., Midya, J., Kappel, M., Butt, H.-J. & Nikoubashman, A. Segregation in drying binary colloidal droplets. *ACS Nano* **13**, 4972–4979 (2019).
- Lilin, P. & Bischofberger, I. Criteria for crack formation and air invasion in drying colloidal suspensions. *Langmuir* **38**, 7442 (2022).
- Hatton, B., Mishchenko, L., Davis, S., Sandhage, K. H. & Aizenberg, J. Assembly of large-area, highly ordered, crack-free inverse opal films. *Proc. Natl. Acad. Sci.* **107**, 10354–10359 (2010).
- Manoharan, V. N. Colloidal matter: Packing, geometry, and entropy. *Science* **349**, 1253751 (2015).
- Pillitteri, S., Lumay, G., Opsomer, E. & Vandewalle, N. From jamming to fast compaction dynamics in granular binary mixtures. *Sci. Rep.* **9**, 1–7 (2019).
- Pillitteri, S., Opsomer, E., Lumay, G. & Vandewalle, N. How size ratio and segregation affect the packing of binary granular mixtures. *Soft Matter* **16**, 9094–9100 (2020).
- Inoue, K. & Inasawa, S. Positive and negative birefringence in packed films of binary spherical colloidal particles. *RSC Adv.* **10**, 2566–2574 (2020).
- Hwang, M.-S. *et al.* Inkjet-printing of nonsintered alumina-resin hybrid films and their dielectric properties. *J. Appl. Phys.* **108**, 102809 (2010).
- Fernandez, F. D. M., Bissannagari, M. & Kim, J. Fully inkjet-printed batio₃ capacitive humidity sensor: Microstructural engineering of the humidity sensing layer using bimodal ink. *Ceram. Int.* **47**, 24693–24698 (2021).
- Buchheit, R., Kuttich, B., González-García, L. & Kraus, T. Hybrid dielectric films of inkjet-printable core-shell nanoparticles. *Adv. Mater.* **33**, 2103807 (2021).
- Yu, Y.-S., Wang, M.-C. & Huang, X. Evaporative deposition of polystyrene microparticles on pdms surface. *Sci. Rep.* **7**, 1–9 (2017).
- Cui, L. *et al.* Suppression of the coffee ring effect by hydrosoluble polymer additives. *ACS Appl. Mater. Interfaces* **4**, 2775–2780 (2012).
- Lee, M. *et al.* Water droplet evaporation from sticky superhydrophobic surfaces. *Appl. Phys. Lett.* **111**, 021603 (2017).
- Dicuangco, M., Dash, S., Weibel, J. A. & Garimella, S. V. Effect of superhydrophobic surface morphology on evaporative deposition patterns. *Appl. Phys. Lett.* **104**, 201604 (2014).
- Jin, H., Li, Y., Zhang, P., Nie, S. & Gao, N. The investigation of the wetting behavior on the red rose petal. *Appl. Phys. Lett.* **108**, 151605 (2016).
- Zhang, C. *et al.* Spectroscopy-assisted label-free molecular analysis of live cell surface with vertically aligned plasmonic nanopillars. *Small* **17**, 2100161 (2021).
- Gustafsson, L., Jansson, R., Hedhammar, M. & van der Wijngaart, W. Structuring of functional spider silk wires, coatings, and sheets by self-assembly on superhydrophobic pillar surfaces. *Adv. Mater.* **30**, 1704325 (2018).
- Tan, S. H., Nguyen, N.-T., Chua, Y. C. & Kang, T. G. Oxygen plasma treatment for reducing hydrophobicity of a sealed polydimethylsiloxane microchannel. *Biomicrofluidics* **4**, 032204 (2010).
- Tabaei, P. S. E. *et al.* Comparative study between in-plasma and post-plasma chemical processes occurring at the surface of uhmwpe subjected to medium pressure ar and n₂ plasma activation. *Polymer* **193**, 122383 (2020).
- Lim, S. J. *et al.* Hydrophobicity evolution on rough surfaces. *Langmuir* **36**, 689–696 (2020).
- Sowade, E., Blaudeck, T. & Baumann, R. R. Inkjet printing of colloidal nanospheres: Engineering the evaporation-driven self-assembly process to form defined layer morphologies. *Nanoscale Res. Lett.* **10**, 1–9 (2015).
- Oh, G., Jeong, W., Jung, N., Kang, S. H. & Weon, B. M. Evaporation and deposition of colloidal binary droplets. *Phys. Rev. Appl.* **17**, 024010 (2022).
- Gonçalves, M. *et al.* Droplet evaporation on porous fabric materials. *Sci. Rep.* **12**, 1–11 (2022).
- Ren, P. *et al.* Achieving high-resolution electrohydrodynamic printing of nanowires on elastomeric substrates through surface modification. *ACS Appl. Electron. Mater.* **3**, 192–202 (2020).
- Chen, F. *et al.* Stability of plasma treated superhydrophobic surfaces under different ambient conditions. *J. Colloid Interface Sci.* **470**, 221–228 (2016).
- Murakami, T., Kuroda, S.-I. & Osawa, Z. Dynamics of polymeric solid surfaces treated with oxygen plasma: Effect of aging media after plasma treatment. *J. Colloid Interface Sci.* **202**, 37–44 (1998).
- Sanchis, M., Calvo, O., Fenollar, O., García, D. & Balart, R. Characterization of the surface changes and the aging effects of low-pressure nitrogen plasma treatment in a polyurethane film. *Polym. Test.* **27**, 75–83 (2008).

37. Waters, L. J., Finch, C. V., Bhuiyan, A. M. H., Hemming, K. & Mitchell, J. C. Effect of plasma surface treatment of poly (dimethylsiloxane) on the permeation of pharmaceutical compounds. *J. Pharm. Anal.* **7**, 338–342 (2017).
38. Qin, Y., Alam, A. U., Howlader, M. M., Hu, N.-X. & Deen, M. J. Morphology and electrical properties of inkjet-printed palladium/palladium oxide. *J. Mater. Chem. C* **5**, 1893–1902 (2017).
39. Kumar, A. & Raj, R. Droplets on microdecorated surfaces: Evolution of the polygonal contact line. *Langmuir* **33**, 4854–4862 (2017).
40. Xu, L., Davies, S., Schofield, A. B. & Weitz, D. A. Dynamics of drying in 3d porous media. *Phys. Rev. Lett.* **101**, 094502 (2008).
41. Patil, N. D., Bhardwaj, R. & Sharma, A. Self-sorting of bidispersed colloidal particles near contact line of an evaporating sessile droplet. *Langmuir* **34**, 12058–12070 (2018).
42. Hu, Y., Zhao, B., Lin, S., Deng, X. & Chen, L. Evaporation and particle deposition of bi-component colloidal droplets on a superhydrophobic surface. *Int. J. Heat Mass Transf.* **159**, 120063 (2020).
43. Xu, Y. & Chung, D. Increasing the thermal conductivity of boron nitride and aluminum nitride particle epoxy-matrix composites by particle surface treatments. *Compos. Interfaces* **7**, 243–256 (2000).
44. Yung, K. C. & Liem, H. Enhanced thermal conductivity of boron nitride epoxy-matrix composite through multi-modal particle size mixing. *J. Appl. Polym. Sci.* **106**, 3587–3591 (2007).
45. He, G., Zhu, L., Liu, M., Fang, Q. & Zhang, L. Optical and electrical properties of plasma-oxidation derived hfo2 gate dielectric films. *Appl. Surf. Sci.* **253**, 3413–3418 (2007).

Acknowledgements

This research was supported by Basic Science Research Program (2016R1D1A1B01007133) and through the National Research Foundation of Korea (NRF) funded by the Ministry of Education (2019R1A6A1A03033215) and the Korea Evaluation Institute of Industrial Technology funded by the Ministry of Trade, Industry and Energy (20000423, Developing core technology of materials and processes for control of rheological properties of nanoink for printed electronics) and the Global Energy Materials Innovator (20194010000290) funded by the Korea Institute of Energy Technology Evaluation and Planning (KETEP).

Author contributions

H.K., M.G., and B.M.W. conceived the experiments. H.K. and M.G. conducted the experiments. H.K., M.G., B.M.W., and S.H.K. analyzed the results. H.K., M.G., B.M.W., and S.H.K. wrote the main manuscript. All authors reviewed the manuscript.

Competing interests

The authors declare no competing interests.

Additional information

Supplementary Information The online version contains supplementary material available at <https://doi.org/10.1038/s41598-022-26151-9>.

Correspondence and requests for materials should be addressed to S.H.K. or B.M.W.

Reprints and permissions information is available at www.nature.com/reprints.

Publisher's note Springer Nature remains neutral with regard to jurisdictional claims in published maps and institutional affiliations.



Open Access This article is licensed under a Creative Commons Attribution 4.0 International License, which permits use, sharing, adaptation, distribution and reproduction in any medium or format, as long as you give appropriate credit to the original author(s) and the source, provide a link to the Creative Commons licence, and indicate if changes were made. The images or other third party material in this article are included in the article's Creative Commons licence, unless indicated otherwise in a credit line to the material. If material is not included in the article's Creative Commons licence and your intended use is not permitted by statutory regulation or exceeds the permitted use, you will need to obtain permission directly from the copyright holder. To view a copy of this licence, visit <http://creativecommons.org/licenses/by/4.0/>.

© The Author(s) 2022